A00-31136

AIAA 2000-2009

Computation of the sound radiated by a 3-D jet using Large Eddy Simulation

C. Bogey, C. Bailly and D. Juvé

Ecole Centrale de Lyon & UMR CNRS 5509
France

6th AIAA/CEAS Aeroacoustics Conference
12-14 June 2000 / Lahaina, Hawaii

AIAA 2000-2009

Computation of the sound radiated by a 3-D jet using Large Eddy Simulation*

Christophe Bogey[†] Christophe Bailly[‡] and Daniel Juvé[§]

Laboratoire de Mécanique des Fluides et d'Acoustique
Ecole Centrale de Lyon & UMR CNRS 5509
BP 163, 69131 Ecully cedex, France.

Abstract

A Large Eddy Simulation (LES) of a subsonic round jet with a Mach number of 0.9 and a Reynolds number of 65000 is presented. The numerical code is built using specific techniques of Computational AeroAcoustics (CAA), in order to provide directly the radiated sound field on a computational domain including the acoustic far-field. The aim of this study is to show the feasibility of LES combined with CAA methods, to determine for a subsonic jet both the turbulent flow and the radiated acoustic field with a high accuracy. The aerodynamic properties of the jet, such as meanflow parameters and turbulent intensities, are in very good agreement with experimental data. The sound field generated by the jet is obtained directly in the simulation and investigated. Acoustic sources in the jet are located around the end of the potential core, consistently with experimental observations. Radiation directivity and sound levels are compared successfully with corresponding measurements.

1. Introduction

Reduction of jet noise requires reliable prediction methods accounting for all phenomena responsible for sound generation and propagation. Since acoustic sources are found in turbulent regions, it is necessary to know precisely the aerodynamic field to identify noise generation mechanisms. Also properties of the acoustic fluctuations, such as the long-range propagation of sound waves, are greatly different from those of the aerodynamic field. Thus approaches specific to aeroacoustics have been developed.

Initially, hybrid approaches such as Lighthill's analogy[1] have been proposed, consisting of two-step calculations separating noise generation and propagation. The aerodynamic field is determined in a first step, and introduced as acoustic source terms in a sound propagation method to obtain the noise radiation in a second step.[2] This approach allows one to use methods well suited to the aerodynamic and acoustic calculations respectively. But it has also two failures restricting its application: the first one is associated with the modelling of source terms, and the second one with the acoustic-flow interactions which are generally not included properly in the wave operator.

An alternative to hybrid approaches, linked to recent progress in numerical simulation, is the direct calculation of sound from the resolution of the compressible Navier-Stokes equations. The objective is to determine both the aerodynamic field and the acoustic waves directly. The computed acoustic field is a priori exact because no acoustic model is used, and all flow effects on wave propagation are taken into account. However, this direct acoustic approach must face serious numerical issues,[3] owing to the great disparity of levels and length scales between the acoustic and aerodynamic fields. This has led to the development of techniques specific to Computational AeroAcoustics (CAA), such as non dispersive and non dissipative numerical schemes, or non-reflective boundary conditions. The challenge is to implement them in Navier-Stokes simulations to compute both the turbulent flow and the radiated acoustic field.

The direct calculation of sound must also naturally meet the difficulties of three-dimensional flow simulations. Three approaches are commonly used to solve the Navier-Stokes equations. The first one, the Direct Numerical Simulation (DNS), consists in calculating all turbulent scales. It was applied suc-

[†]Postdoctoral Student, Member AIAA

[‡]Assistant Professor, Member AIAA

[§]Professor, Member AIAA

cessfully by Freund *et al.*[4,5] to determine the noise radiated by supersonic and subsonic round jets. Nevertheless, DNS is restricted to low Reynolds numbers, and turbulence modelling is necessary to simulate higher Reynolds number flows characterized by a wider range of scales. In Large Eddy Simulation (LES), only larger scales are calculated whereas the effects of smaller ones are assigned to a subgrid scale model. It is also possible to solve the unsteady Reynolds Averaged Navier-Stokes equations (RANS) using turbulence closures. Applications of these last two methods have been investigated respectively by Morris *et al.*,[6] with the calculation by LES of the radiation of a supersonic rectangular jet, and by Shen & Tam,[7] with the study of screech tones generation in a round jet using unsteady RANS. These approaches are still to be applied very carefully, because the modelling of a part of the turbulence is likely to modify aerodynamic sound sources.

In this study, a Large Eddy Simulation of a subsonic round jet, with a Mach number of 0.9 and a Reynolds number of 65000 is performed. It is the natural continuation in 3-D of a preliminary work dealing with the computation of the sound radiated by a subsonic mixing layer using the ALESIA code.[8] The aim is, by making use of CAA methods in a Large Eddy Simulation, to obtain for a subsonic jet the aerodynamic flow properties as well as the radiated sound field, and to validate both of them by comparison with experimental data.

This paper is organized as follows. Governing equations and numerical techniques implemented in the ALESIA code are presented in section 2. In section 3, we describe the jet characteristics and the simulation parameters. Next, aerodynamic results are shown in section 4. Then, the radiated acoustic field is investigated in section 5. Finally, concluding remarks are given in section 6.

2. Numerical simulation algorithm

2.1 Governing equations

The full three-dimensional Navier-Stokes equations are written in a conservative form. In cartesian coordinates, we have

$$\frac{\partial \mathbf{U}}{\partial t} + \frac{\partial \mathbf{Ee}}{\partial x_1} + \frac{\partial \mathbf{Fe}}{\partial x_2} + \frac{\partial \mathbf{Ge}}{\partial x_3} - \frac{\partial \mathbf{Ev}}{\partial x_1} - \frac{\partial \mathbf{Fv}}{\partial x_2} - \frac{\partial \mathbf{Gv}}{\partial x_3} = 0 \qquad (1)$$

The unknown vector $\mathbf{U}$ is given by

$$\mathbf{U} = (\rho, \rho u_1, \rho u_2, \rho u_3, \rho e)^t$$

where ρ, u_1, u_2, u_3, and e are the density, the three velocity components, and the total specific energy respectively. Euler and viscous fluxes in the three coordinate directions are denoted by the subscripts e and v. System (1) is completed by the definition of the total specific energy for a perfect gas

$$\rho e = \frac{p}{\gamma - 1} + \frac{1}{2}\rho(u_1^2 + u_2^2 + u_3^2)$$

where γ is the specific heat ratio, and p the pressure. Thus Euler fluxes are written as

$$\mathbf{Ee} = \begin{pmatrix} \rho u_1 \\ p + \rho u_1^2 \\ \rho u_1 u_2 \\ \rho u_1 u_3 \\ (\rho e + p) u_1 \end{pmatrix} \qquad \mathbf{Fe} = \begin{pmatrix} \rho u_2 \\ \rho u_1 u_2 \\ p + \rho u_2^2 \\ \rho u_2 u_3 \\ (\rho e + p) u_2 \end{pmatrix}$$

$$\mathbf{Ge} = \begin{pmatrix} \rho u_3 \\ \rho u_1 u_3 \\ \rho u_2 u_3 \\ p + \rho u_3^2 \\ (\rho e + p) u_3 \end{pmatrix}$$

and viscous fluxes as

$$\begin{cases} \mathbf{Ev} = (0, \tau_{11}, \tau_{12}, \tau_{13}, u_i \tau_{1i})^t \\ \mathbf{Fv} = (0, \tau_{21}, \tau_{22}, \tau_{23}, u_i \tau_{2i})^t \\ \mathbf{Gv} = (0, \tau_{31}, \tau_{32}, \tau_{33}, u_i \tau_{3i})^t \end{cases}$$

The viscous stress tensor τ_{ij} is defined by $\tau_{ij} = 2\mu S_{ij}$ where μ is the dynamic molecular viscosity, and S_{ij} the deviatoric part of the deformation stress tensor given by

$$S_{ij} = \frac{1}{2}\left(\frac{\partial u_i}{\partial x_j} + \frac{\partial u_j}{\partial x_i} - \frac{2}{3}\delta_{ij}\frac{\partial u_k}{\partial x_k}\right)$$

2.2 Numerical scheme

The numerical algorithm experimented to solve the 2-D Navier-Stokes equations[8] is implemented in the 3-D case. This high-order, non-dispersive and non-dissipative, scheme has shown in 2-D its capacity to compute the sound waves with accuracy, despite the difference of magnitude between aerodynamic and acoustic fields. It combines the DRP scheme of Tam & Webb[9] for space discretization with a fourth-order Runge-Kutta algorithm for time integration. A selective damping[3] is also used to filter out short waves not supported by the scheme.

The mesh is non uniform, because different discretizations are required in the aerodynamic near-field and in the acoustic far-field.

2.3 Boundary Conditions

The 2-D formulation proposed by Tam & Dong[10] is extended to the 3-D case. These boundary conditions are built from the asymptotic solution of Euler's equations in the acoustic far-field, and allow to minimize acoustic reflexions generated when fluctuations leave out the computational domain.

Into the inflow and the lateral sides of the computational domain, only acoustic fluctuations are reaching the boundaries. Radiation boundary conditions, defined by the differential system governing the behaviour of acoustic perturbations in the far-field, are thus applied. They are written, in spherical coordinates, as

$$\frac{1}{v_g}\frac{\partial}{\partial t}\begin{pmatrix} \rho \\ u_1 \\ u_2 \\ u_3 \\ p \end{pmatrix} + \left(\frac{\partial}{\partial r} + \frac{1}{r}\right)\begin{pmatrix} \rho - \overline{\rho} \\ u_1 - \overline{u}_1 \\ u_2 - \overline{u}_2 \\ u_3 - \overline{u}_3 \\ p - \overline{p} \end{pmatrix} = 0$$

where v_g is the acoustic group velocity, and $\overline{\rho}$, $\overline{u}_1$, $\overline{u}_2$, $\overline{u}_3$ and $\overline{p}$ are the mean density, velocity components and pressure respectively. These mean quantities are computed during the simulation.

Into the outflow, aerodynamic fluctuations convected by the flow are also leaving the computational domain. The first four equations are modified to enable the exit of vortical or entropic perturbations. The outflow boundary conditions are written as

$$\left\{\begin{array}{l} \dfrac{\partial \rho}{\partial t} + \overline{\mathbf{u}}.\nabla\left(\rho - \overline{\rho}\right) = \dfrac{1}{\overline{c}^2}\left(\dfrac{\partial p}{\partial t} + \overline{\mathbf{u}}.\nabla\left(p - \overline{p}\right)\right) \\[2ex] \dfrac{\partial u_i}{\partial t} + \overline{\mathbf{u}}.\nabla\left(u_i - \overline{u}_i\right) = -\dfrac{1}{\overline{\rho}}\dfrac{\partial\left(p - \overline{p}\right)}{\partial x_i} \quad [i = 1,2,3] \\[2ex] \dfrac{1}{v_g}\dfrac{\partial p}{\partial t} + \dfrac{\partial\left(p - \overline{p}\right)}{\partial r} + \dfrac{\left(p - \overline{p}\right)}{r} = 0 \end{array}\right.$$

where $\overline{c} = \sqrt{\gamma\overline{p}/\overline{\rho}}$ is the mean sound speed.

The efficiency of the boundary conditions is estimated with two test cases.[11] The first case is a purely acoustic problem with the propagation of a three-dimensional acoustical pulse in an uniform Mach 0.5 flow. Acoustic perturbations are leaving out the computational domain without significant reflexions. In the second one, aerodynamic perturbations are considered with the convection of a vortex ring in a uniform Mach 0.5 flow. The exit of this vortical structure generates weak spurious waves, but which are not negligible in comparison with the physical sound field characterized by small amplitudes. Similar results were found for the 2-D formulation of Tam & Dong boundary conditions.[11] A sponge zone is therefore implemented in the outflow direction to dissipate aerodynamic fluctuations before they reach the boundary, and to filter out possible reflected waves.[8] It is based on the combination of grid stretching with the introduction of an artificial damping term in system (1).

2.4 Subgrid Scale Model

The resolution of Navier-Stokes equations requires the calculation of all turbulent scales. These Direct Numerical Simulations (DNS) are thus restricted to low Reynolds number flows.

To simulate flows at higher Reynolds number, a possibility is to compute only the larger structures, and to take into account of the effects of smaller scales via a subgrid scale model. This method is referred to as Large Eddy Simulation (LES). A turbulent viscosity μ_t ensures dissipation of the smaller unresolved structures. Basically, μ is replaced by $\mu + \mu_t$ in system (1). Various models have been built to determine an expression of this turbulent viscosity. To keep the problem as simple as possible for aerodynamics, we choose Smagorinsky's model[12]

$$\mu_t = \rho\left(C_s\Delta_c\right)^2\sqrt{2S_{ij}S_{ij}}$$

where the Smagorinsky constant is taken to be $C_s = 0.18$, and the characteristic grid length is

$$\Delta_c = \sqrt[3]{\Delta x_1 \Delta x_2 \Delta x_3}$$

3. Flow simulation

3.1 Flow parameters

The inflow axial velocity $u(r)$ of the jet is given by the following hyperbolic-tangent profile

$$u(r) = \frac{U_j}{2} + \frac{U_j}{2}\tanh\left(\frac{r_0 - r}{2\delta_\theta}\right)$$

where U_j is the inflow centerline velocity, δ_θ the initial momentum thickness of the shear layer, and r_0 the jet radius.

The jet Mach number M_j is taken as 0.9, and the fluid surrounding the jet is initially at rest. The choice of this Mach number is justified by the amount of experimental studies available in the literature, providing both aerodynamic results,[13] and acoustic results.[14-16] This Mach number allows also a high convection speed of turbulent structures, which reduces computation time. We can notice that the first numerical simulation of a subsonic jet to determine directly its radiated field involves a Mach number 0.9 jet. It is the DNS of a Reynolds number 3600 jet carried out by Freund.[5]

The jet Reynolds number, based on the jet diameter and defined by $Re_D = U_j \times D/\nu$, is equal to $Re_D = 65000$. It is higher than Reynolds numbers affordable in DNS, but still lower than values of practical interest, typically $Re_D \geq 10^5$.

The ratio between the initial jet radius and the initial momentum thickness of the shear layer is also an important parameter. Transition from laminar flow to a fully turbulent jet is greatly dependent on its value. In this study, the ratio δ_θ/r_0 is 0.05, that enables the development of vortical structures in the shear zones, before turbulent mixing occurs on the whole radial section of the jet corresponding to the end of the potentiel core.

3.2 Numerical specifications

The computational mesh consists of $255 \times 187 \times 127$ points in the three coordinate directions. Owing to computer limitations inherent in 3-D calculations, meshes are significantly stretched as represented in Figure 1.

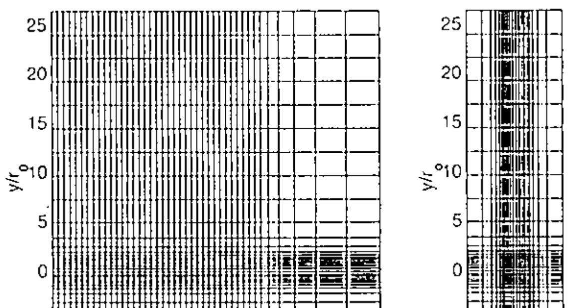

Figure 1: Visualization of the $x-y$ and $y-z$ sections of the cartesian mesh grid. Only every sixth line in the three coordinate directions is shown.

Points are clustered radially in the jet, with 26 points in the initial jet radius. The minimum mesh spacing Δ_0, found around $r = r_0$, is chosen to be $\delta_\theta = 1.6\Delta_0$, so that there are about ten grid points in the initial shear. Outside the jet, mesh spacing increases rapidly, to reach a value of $\Delta y_{max} = 0.4r_0$ in the far-field. This mesh spacing Δy_{max} allows an accurate sound propagation up to a frequency corresponding to a cut-off Strouhal number $St_c = f_c \times D/U_j \simeq 1.1$.

In the flow direction, mesh spacing is constant up to $x = 20r_0$, with $\Delta x = 3\Delta_0$. Then, meshes are stretched for the 40 last points with $\Delta x_{max} = 0.54r_0$, in order to build up a sponge zone. Following the technique used in a previous study,[8] an artificial damping term is progressively added in the sponge zone. It is only applied in the flow region using a radial weighting. Thus, the physical part of the computational domain extends in the axial direction up to $x = 20r_0$ for the aerodynamic field, and up to $x = 30r_0$ for the acoustic far-field.

The mesh grid is refined enough to calculate accuratly large turbulent structures. The subgrid scale viscosity is around 10 times the molecular viscosity, which is small compared to values usually found. That may prevent the subgrid model from being unsuited or from generating parasitic noise.

The time step is defined by $\Delta t = 0.7\Delta_0/c_0$. The selective damping is applied two times per iteration with a mesh Reynolds number $R_s = 5$, to ensure the numerical stability of the simulation in presence of three-dimensional turbulence. The simulation runs for 30000 iterations, the calculation of statistical means starting after 5000 iterations. Consequently, the simulation time corresponds to $22 \times Lx/c_0$, where $Lx = 30r_0$ is the grid length in the axial direction. The computation is 15 hours long on a Nec SX-5, with a CPU time of $0.3\mu s$ per grid point and per iteration, and a CPU speed of 5000 Mflops.

3.3 Inflow forcing

The jet is forced using a random excitation to obtain its natural development. Velocity fluctuations are added into the inflow to seed the turbulence in the jet. They are solenoïdal in order to minimize the production of spurious acoustic waves. These vortical perturbations are generated by the following process.

First a vortex ring of radius r_0 is built up near the inflow at $x = 0.8r_0$. It has a longitudinal and and a radial velocity, but no azimuthal one. The n^{th} spatial mode of the excitation is then obtained from this basic vortex ring by multiplying with the function $\cos(n\theta)$. In this study, the jet is excited using the first tenth modes.

This ring excitation is only applied in the shear layer, that is the most unstable region of the jet. In these shear zones, turbulent intensities generated by the forcing are around 3%, which is similar to intensities observed experimentally at jet nozzle exits.

Thus, it allows to start properly the transition to turbulence in the jet.

4. Aerodynamic results

4.1 Flow development

Figure 2 displays the vorticity fields provided by LES. The longitudinal vorticity field ω_{xy} shows that vortical structures are generated in the two shear layers, which grow initially rather independently. The shear zones begin to interact in the vicinity of $x = 10r_0$, indicating the end of the potential core of the jet. Then, a developed turbulence is found downstream, illustrated by the transversal vorticity field ω_{yz}, and characterized by a typical three-dimensional mixing. We can also observe that aerodynamic fluctuations are dissipated by the sponge zone from $x = 20r_0$.

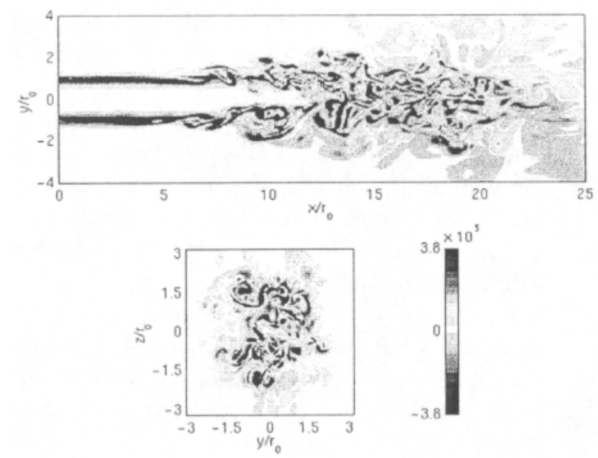

Figure 2: Snapshots of the vorticity field. Upper picture, ω_{xy} in the $x-y$ plane at $z=0$; bottom picture, ω_{yz} in the $y-z$ plane at $x = 12r_0$. Levels are given in s^{-1}.

4.2 Mean flow properties

Contours of the mean longitudinal velocity are shown in Figure 3 for velocities varying from 0.05 U_j up to 0.95 U_j. The jet potential core, region of uniform velocity equal to U_j, can be seen. Its end is located around $x = 10r_0$, which is in agreement with experimental values. For exemple, Lau *et al.*[13] have observed the end of the potential core of a Mach 0.9 jet at a distance of $10.4r_0$ from the nozzle exit.

Mean streamlines are also plotted in Figure 3. Surrounding fluid, initially at rest, is drawn radially to the flow direction, at a low speed of the order of 2% U_j. Then the fluid is carried away in the jet. It is in accordance with experimental descriptions of fluid entrainment mechanism, responsible for the increase of jet flow rate.[21] The boundary conditions implemented in the simulation allow the incoming of fluid in the computational domain to feed the flow. This result is essential to obtain flow characteristics conform to experiments.

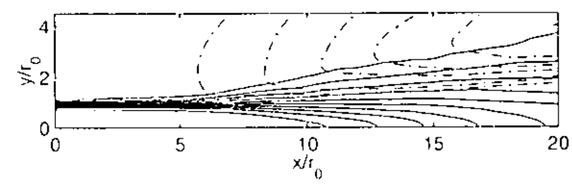

Figure 3: Visualization of mean flow: ——— , 10 contours of the mean longitudinal velocity defined from 0.05 to 0.95 U_j; — · — · , 5 mean streamlines.

Figures 4 illustrates computed mean flow properties. In particular, the linear growth of different mean parameters is found in the jet region where turbulence is developed, which corresponds to the assumption of self-similar mean profiles.

In this region, the mean centerline velocity U_c follows a x^{-1} decay in the axial direction, which can be written as

$$\frac{U_c}{U_j} = B \times \frac{D}{x - x_0}$$

where x_0 is the virtual origin, and B is the decay constant. Figure 4(a) presents the longitudinal evolution of the inverse of the mean centerline velocity normalized with the inflow velocity U_j. Its value is 1 in the potential core, and it grows linearly afterwards, confirming the x^{-1} decay of U_c. The constant B is 5.5, with a virtual origin at $x_0 = 0$. It is consistent with measurements of Wygnanski & Fiedler,[17] Panchapakesan & Lumley[18] and Hussein *et al.*,[19] as well as DNS results of Boersma *et al.*,[20] reported in Table 1.

Re_D	B	A	Reference
8.6×10^4	5.4	0.086	Wygnanski *et al.*[17]
1.1×10^4	6.1	0.096	Panchapakesan *et al.*[18]
9.5×10^4	5.8	0.094	Hussein *et al.*[19]
2.4×10^3	5.9	0.095	Boersma *et al.*[20]
6.5×10^4	5.5	0.096	Present simulation

Table 1: Mean flow parameters obtained from different experiments, DNS, and present simulation.

In the same way, the half-width of the jet $\delta_{1/2}$, defined as the distance from the axis for which the

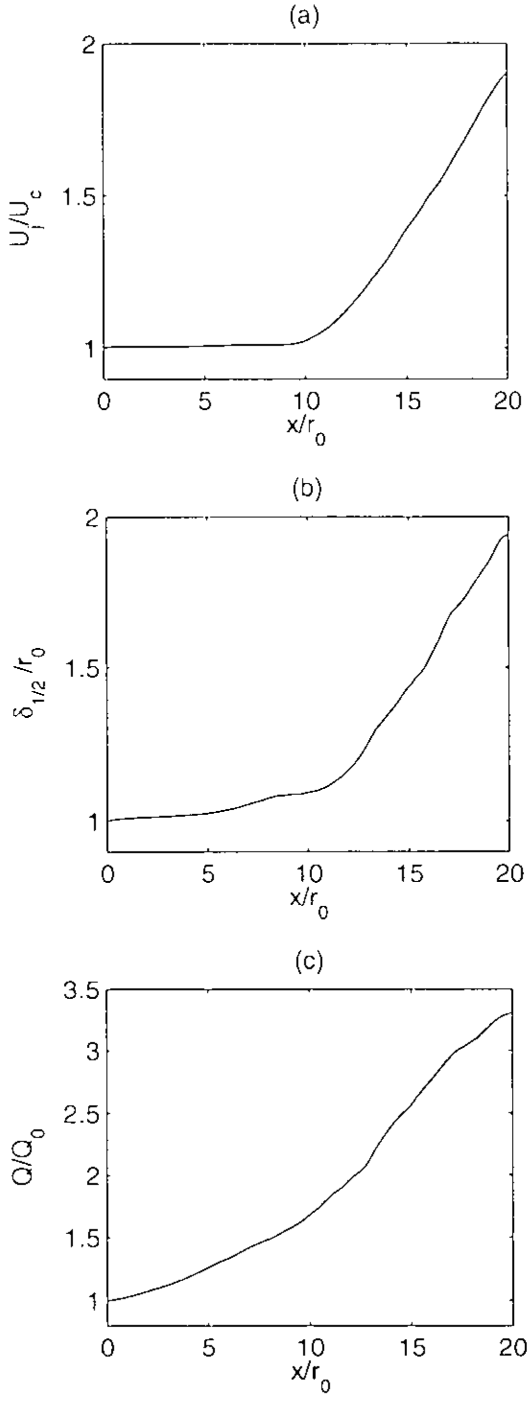

Figure 4: Longitudinal evolution of: (a), the inverse of the mean centerline velocity normalized with the inflow velocity U_j/U_c; (b), the half-width of the jet normalized with the jet radius δ_{12}/r_0; (c), the mean flow rate normalized with the inflow rate Q/Q_0.

mean longitudinal velocity is half the centerline velocity, grows linearly in the jet self-similar region as

$$\delta_{1/2} = A \times (x - x_0) \quad .$$

where A is the spreading rate of the jet. In Figure 4(b), we show the longitudinal evolution of the jet half-width normalized with the initial radius r_0. Its value is 1 as long as no vortical structures are created in the shear layers, and then increases slowly at their appearance around $x = 6r_0$. Afterwards, the jet spreads linearly in the turbulent region, with a rate A equal to 0.096, that is in agreement with experimental and numerical data of Table 1.

Finally, owing to the x^{-1} decay of the centerline velocity and to the linear spreading of the jet, the axial mean flow rate Q must also grow linearly as

$$\frac{Q}{Q_0} = C \times \frac{x - x_0}{D}$$

where Q_0 is the inflow rate, and C is the entrainment rate. Figure 4(c) displays the longitudinal evolution of the mean flow rate normalized with Q_0. This ratio grows regularly, since the entrainment of the surrounding fluid occurs from the inflow of the computational domain. Nevertheless, the growth is linear only after the end of the potential core, with an entrainment rate C around 0.32. Experimental values of the entrainment rates are rare in the literature, because they are difficult to measure. Ricou & Spalding[21] have however succeeded in determining the mass entrainment rates of jets between different fluids. In the air-air case, they have found a rate of 0.32, which is the same as that given by the simulation.

The mean velocity properties of the jet calculated by LES are therefore in very good agreement with corresponding data available in the literature.

4.3 Turbulent intensities

Turbulent intensities of aerodynamic perturbations provided by LES are now investigated. The longitudinal intensity σ_{uu}, radial intensity σ_{vv} and azimuthal intensity σ_{ww} are calculated in the $x-y$ plane at $z = 0$, using velocity fluctuations u', v' et w'. They are written as

$$\sigma_{uu} = \frac{\sqrt{\overline{u'^2}}}{U_c} \qquad \sigma_{vv} = \frac{\sqrt{\overline{v'^2}}}{U_c} \qquad \sigma_{ww} = \frac{\sqrt{\overline{w'^2}}}{U_c}$$

The turbulent intensity σ_{uv} is also defined by

$$\sigma_{uv} = \frac{\sqrt{|\overline{u'v'}|}}{U_c}$$

These intensities are normalized with the local centerline longitudinal velocity, according to usual representation.

Radial profiles of the four turbulent intensities are shown in Figures 5 and 6 at five locations between $x = 15r_0$ and $x = 20r_0$, as function of the nondimensional coordinate $y/(x - x_0)$. Profiles are well superimposed, in agreement with the self-similarity of fully turbulent jet. The mean profiles calculated between $x = 15r_0$ and $x = 20r_0$ are also plotted as solid lines. Results are very close to measurements, and mean calculated curves stand between two experimental profiles provided by Panchapakesan & Lumley[18] and by Hussein *et al.*[19]

Turbulence levels supplied by the LES are compared successfully with experimental data. In particular, the use of the Smagorinsky subgrid-scale model has not brought a too high dissipation of turbulent structures. This model is actually suited to the jet configuration, where the Boussinesq hypothesis is valid and fine turbulence is quasi isotropic.

4.4 Turbulent spectrum

Turbulence is fully developed at the point located at $y = r_0$, $z = 0$ and $x = 16.8r_0$. The turbulent kinetic energy spectrum $E(k_1)$ is then calculated at this point, and plotted in Figure 7. The Taylor hypothesis of frozen turbulence is applied to estimate $E(k_1)$ from the temporal spectrum $E(f)$. In practice, the usual relation $k_1 = 2\pi f/\overline{u}_1$ is used.

The grid cut-off wave number k_c, is given by $k_c = 2\pi/(6\Delta_c)$, where Δ_c is the local mean mesh spacing. It corresponds to the highest wave number well supported by the numerical algorithm, with 6 points per wavelength. As expected, the spectrum $E(k_1)$ decreases rapidly in the vicinity of k_c. The grid cut-off is also related to a Strouhal number $St_c = 2.5$, so that predominant sound sources, typically found between $0.1 < St < 1$ in a jet, will not be affected significantly by the LES filtering.

The cut-off of the turbulent spectrum is located in the $k^{-5/3}$ inertial zone, where the kinetic energy is transfered from large structures to dissipative fine scales. That is one assumption of the Smagorinsky subgrid scale model.

5. Direct calculation of the acoustic field

5.1 Dilatation field

Figure 8 displays the dilatation field $\Theta = \nabla.\mathbf{u}$ provided directly by LES. Dilatation accounts only for compressible fluctuations, and is also connected

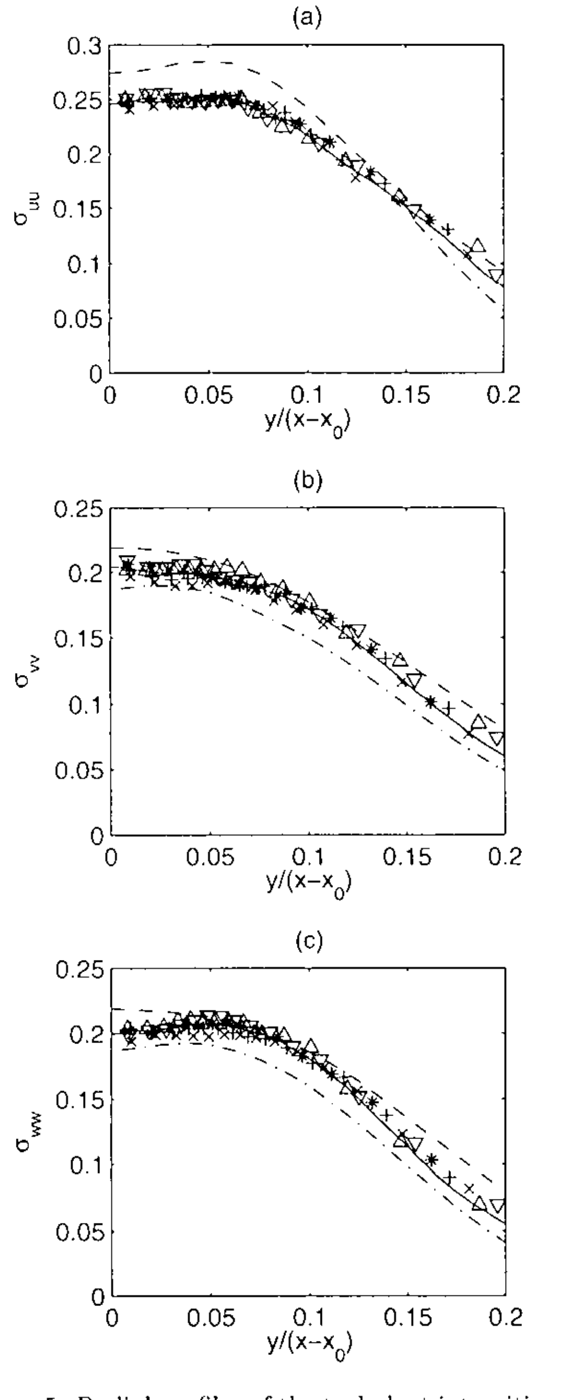

Figure 5: Radial profiles of the turbulent intensities: (a), σ_{uu}; (b), σ_{vv}; (c), σ_{ww}. $\times$, at $x = 15.8r_0$; $+$, at $x = 16.8r_0$; $*$, at $x = 17.7r_0$; ∇, at $x = 18.6r_0$; Δ, at $x = 19.6r_0$. ——— , mean profiles calculated from $x = 15r_0$ to $x = 20r_0$; $- \cdot - \cdot$, experimental profiles obtained by Panchapakesan & Lumley[18]; $- - -$, experimental profiles obtained by Hussein, Capp & George.[19]

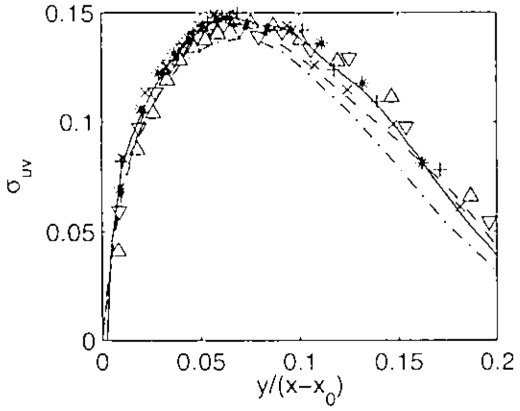

Figure 6: Radial profiles of the turbulent intensity σ_{uv}. See Figure 5 for the meaning of various curves and symbols.

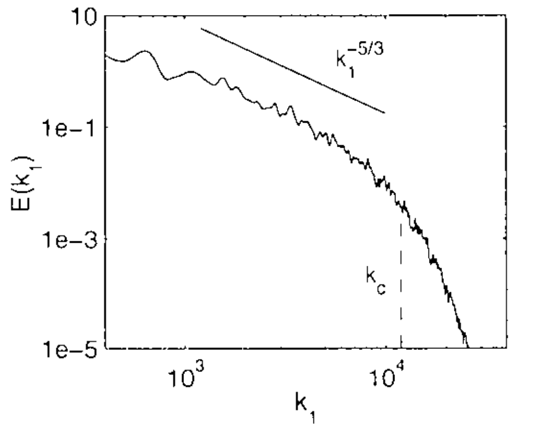

Figure 7: Turbulent kinetic energy spectrum $E(k_1)$ in dB/Hz, at the point located at $x = 16.8r_0$, $y = r_0$ and $z = 0$.

to the acoustic pressure outside the flow region, where the meanflow is negligible, by the formula

$$\Theta = \nabla.\mathbf{u} = -\frac{1}{\rho_0 c_0^2}\frac{\partial p}{\partial t}$$

Dilatation is thus proportional to the time derivative of the acoustic pressure outside the jet. Its use allows to eliminate the mean pressure field, and to filter very low frequency oscillations.

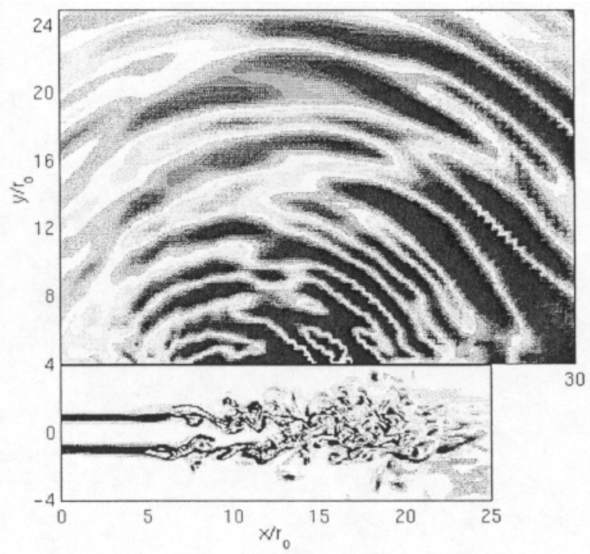

Figure 8: Snapshot of the dilatation field $\Theta = \nabla.\mathbf{u}$ in the acoustic region, and of the vorticity field ω_{xy} in the aerodynamic region, in the $x - y$ plane at $z = 0$. The dilatation color scale is defined for levels from -90 à 90 s^{-1}, the vorticity scale is the same as in Figure 2.

This figure demonstrates that the dilatation field is not contaminated by parasitic waves generated by the inflow excitation or by the exit of turbulent structures of the computational domain. Wave fronts are mainly coming from an origin located around $x = 11r_0$, in the region where the mixing layers are merging. It can be noted that predominant acoustic sources are located around the end of the potential core. This agrees both with the results of the recent DNS performed by Freund[5] and with the measurements of Chu & Kaplan[22] and Juvé *et al.*[23] using various source localization techniques. Moreover, the computed radiated field is more pronounced in the downstream direction, in accordance with experimental directivities.

5.2 Pressure field properties

In order to determine the sound levels, the time evolution of pressure is recorded in the acoustic far-field, at different points along the boundaries of the computational domain. Figure 9 plots the fluctuating pressure obtained during 4000 iterations at $x = 10r_0$, $y = 24r_0$ and $z = 0$. Very low frequency oscillations are visible, with an amplitude higher than that of physical waves. We suppose that these spurious oscillations are due to reflections coming from the outflow boundary. The sponge zone being built up over only 40 points, the low frequency waves supported by the maximum mesh spacing in the longitudinal direction may not be dissipated enough by the artificial damping term.

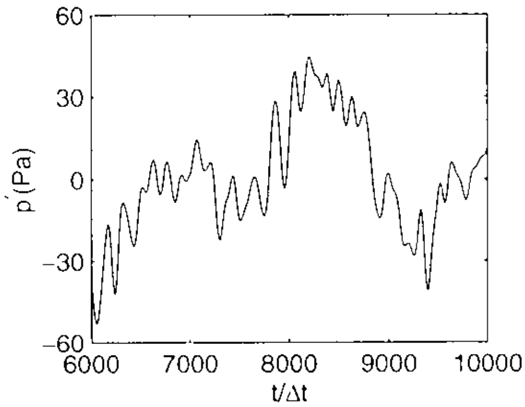

Figure 9: Time evolution of the fluctuating pressure recorded at the point located at $x = 10r_0$, $y = 24r_0$ and $z = 0$, during 4000 iterations.

This property is also observed in Figure 10, presenting the pressure spectrum in dB at the point considered in Figure 9. The spectrum increases rapidly to the low frequencies from a Strouhal number $St \simeq 0.1$. This low frequency behavior was previously found in numerical studies of Zhang *et al.*[24] and of Shieh & Morris[25] dealing with the computation of noise generated by flows past a cavity. Moreover, the spectrum decreases sharply around a Strouhal number of 1, in the vicinity of the grid cut-off frequency in the acoustic far-field. For $0.1 < St < 1$, the spectrum appears actually as a typical jet noise spectrum with a peak around $St \simeq 0.3$.

5.3 Sound pressure level

Following Zhang *et al.*,[24] the physical part and the spurious low frequency part of the spectrum are distinguished to calculate the Sound Pressure Level (SPL). The pressure spectrum is therefore integrated from a Strouhal number $St = 0.15$. The radiation of experimental jets concerns mainly a frequency range of $0.2 < St < 1$.[14-16,23] The sound contribution of the low frequency part of the physical radiated field,

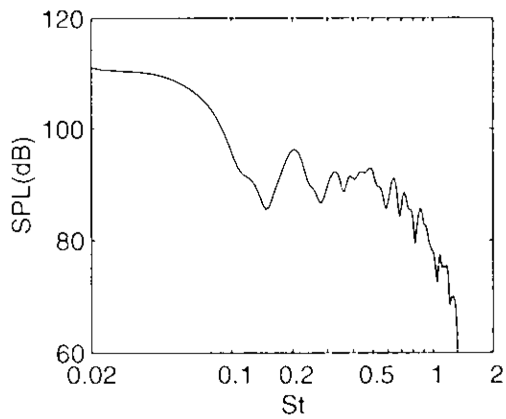

Figure 10: Sound pressure level obtained from the pressure at the point defined in Figure 9, as function of Strouhal number $St = fD/U_j$.

neglected in our calculation, is not predominant. By this way, the computed SPL are very close to those obtained if the whole physical spectrum were integrated.

SPL are estimated at a distance of $60r_0$ from the inflow, to enable the comparison with measurements taking the jet nozzle exit as origin of the directivity. The r^{-1} decay of acoustic waves is used from the sound sources located at $x = 11r_0$ to the different far-field recording points. Figure 11 shows the calculated SPL, and experimental data for various Reynolds numbers, reported in Table 2. The agreement between numerical sound levels and measurements is excellent.

M	Re_D	Reference
0.9	5.4×10^5	Mollo-Christensen *et al.*[14]
0.88	5×10^5	Lush[15]
0.9	3600	Stromberg *et al.*[16]
0.9	6.5×10^4	Present simulation

Table 2: Some jets with Mach numbers similar to the Mach number of the present simulation, for which the radiated sound field has been measured.

The acoustic level reaches a peak around an angle of 30°, and it decreases for angles closer to the jet axis, which can be attributed to flow refraction effects. Furthermore, the acoustic radiation is much more marked in the downsteam direction, with upstream sound levels at least 10 dB inferior to the highest value obtained downstream.

The sound field provided by LES compares successfully with measurements in terms of directivity and levels. Despite the problem associated with the

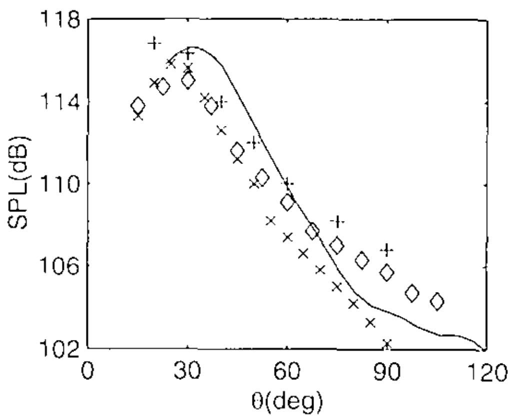

Figure 11: Sound pressure level as function of angle θ measured from the jet axis, at $60r_0$ from the jet nozzle. Experimental data by: +, Mollo-Christensen *et al.*[14]; ◇, Lush[15]; ×, Stromberg *et al.*.[16]

spurious very low frequency oscillations, the radiated field is correctly calculated. Predominant noise generation mechanisms are well described in the numerical simulation. They seem to be relatively independent of the Reynolds number, considering the similarity between the noise radiation of jets with very different Reynolds numbers from 3600 up to 5.4×10^5.

6. Conclusion

In this paper, a Large Eddy Simulation of a 3-D round jet with a Mach number of 0.9 and a Reynolds number of 65000 has been presented. The simulation is based on CAA numerical methods in order to compute directly the aerodynamic noise. Implementation and results of the calculation are presented.

Specific CAA techniques, such as the numerical algorithm or the non-reflecting boundary conditions, initially developed to propagate accuratly sound waves using Linearized Euler's equations, are capable of solving the full Navier-Stokes equations in order to simulate turbulent flows.

Aerodynamic properties of the jet, namely mean-flow parameters and turbulent intensities, are in very good agreement with experimental data of the literature. The acoustic field radiated by the jet is also directly given by the LES. Sound sources in the jet are found at the end of the potential core, as shown experimentally. The integration of the physical spectrum provides sound pressure levels and directivity reproducing well experimental results.

This study shows the feasibility of the direct calculation of the acoustic field generated by subsonic flows using LES. The excellent concordance with measurements supports that aerodynamic and acoustic mechanisms are well accounted for by our simulation. In that way, further works will investigate the generation mechanisms of jet noise.

Acknowledgments

Computing time is supplied by Institut du Développement et des Ressources en Informatique Scientifique (IDRIS - CNRS). Financial support is provided by Electricité de France, Direction des Etudes et Recherches (P. Lafon).

References

[1] LIGHTHILL, M.J., 1952, On sound generated aerodynamically - I. General theory, *Proc. Roy. Soc. London*, **211**, Ser. A, 1107, 564-587.

[2] BASTIN, F., LAFON, P. & CANDEL, S., 1997, Computation of jet mixing noise due to coherent structures: the plane jet case, *J. Fluid Mech.*, **335**, 261-304.

[3] TAM, C.K.W., 1995, Computational aeroacoustics: issues and methods, *AIAA Journal*, **33**(10), 1788-1796.

[4] FREUND, J.B., LELE, S.K. & MOIN, P., 1998, Direct simulation of a Mach 1.92 jet and its sound field, AIAA Paper 98-2291.

[5] FREUND, J.B., 1999, Acoustic sources in a turbulent jet: a direct numerical simulation study, AIAA Paper 99-1858.

[6] MORRIS, P.J., LONG, L.N. & SCHEIDEGGER, T.E., 1999, Parallel computations of high speed jet noise, AIAA Paper 99-1873.

[7] SHEN, H. & TAM, C.K.W., 1998, Numerical simulation of the generation of the axisymmetric mode jet screech tones, *AIAA Journal*, **36**(10), 1801-1807.

[8] BOGEY, C., BAILLY, C. & JUVÉ, D., 1999, Computation of mixing layer noise using Large Eddy Simulation, AIAA Paper 99-1871, accepted in the AIAA Journal.

[9] TAM, C.K.W. & WEBB, J.C., 1993, Dispersion-relation-preserving finite difference schemes for computational acoustics, *J. Comput. Phys.*, **107**, 262-281.

[10]TAM, C.K.W. & DONG, Z., 1996, Radiation and outflow boundary conditions for direct computation of acoustic and flow disturbances in a nonuniform mean flow, *J. Comput. Acous.*, 4(2), 175-201.

[11]BOGEY, C., 2000, Calcul direct du bruit aérodynamique et validation de modèles acoustiques hybrides, Ph. D. Thesis of Ecole Centrale de Lyon, No. 2000-11.

[12]SMAGORINSKY, J.S., 1963, General circulation experiments with the primitive equations: I. the basic experiment, *Mon. Weath. Rev.*, **91**, 99-163.

[13]LAU, J.C., MORRIS, P.J. & FISHER, M.J., 1979, Measurements in subsonic and supersonic free jets using a laser velocimeter, *J. Fluid Mech.*, **93**(1), 1-27.

[14]MOLLO-CHRISTENSEN, E., KOLPIN, M.A. & MARTUCELLI, J.R., 1964, Experiments on jet flows and jet noise far-field spectra and directivity patterns, *J. Fluid Mech.*, **18**, 285-301.

[15]LUSH, P.A., 1971, Measurements of subsonic jet noise and comparison with theory, *J. Fluid Mech.*, **46**(3), 477-500.

[16]STROMBERG, J.L., MCLAUGHLIN, D.K. & TROUTT, T.R., 1980, Flow field and acoustic properties of a Mach number 0.9 jet at a low Reynolds number, *J. Sound Vib.*, **72**(2), 159-176.

[17]WYGNANSKI, I. & FIEDLER, H., 1969, Some measurements in the self-preserving jet, *J. Fluid Mech.*, **38**(3), 577-612.

[18]PANCHAPAKESAN, N.R. & LUMLEY, J.L., 1993, Turbulence measurements in axisymmetric jets of air and helium. Part I. Air jet. *J. Fluid Mech.*, **246**, 197-223.

[19]HUSSEIN, H.J., CAPP, S.P. & GEORGE, W.K., 1994, Velocity measurements in a high-Reynolds-number, momentum-conserving, axisymmetric, turbulent jet, *J. Fluid Mech.*, **258**, 31-75.

[20]BOERSMA, B.J., BRETHOUWER, G. & NIEUWSTADT, F.T.M., 1998, A numerical investigation on the effect of the inflow conditions on a self-similar region of a round jet, *Phys. Fluids*, **10**(4), 899-909.

[21]RICOU, F.P. & SPALDING, D.B., 1961, Measurements of entrainment by axisymmetrical turbulent jets, *J. Fluid Mech.*, **11**, 21-32.

[22]CHU, W.T. & KAPLAN, R.E., 1976, Use of a spherical concave reflector for jet-noise-source distribution diagnosis, *J. Acoust. Soc. Am.*, **59**(6), 1268-1277.

[23]JUVÉ, D., SUNYACH, M. & COMTE-BELLOT, G., 1980, Intermittency of the noise emission in subsonic cold jets, *J. Sound Vib.*, **71**(3), 319-332.

[24]ZHANG, X., RONA, A. & LILLEY, G.M., 1995, Far-field radiation from an unsteady supersonic cavity flow, AIAA Paper 95-040.

[25]SHIEH, C.M. & MORRIS, P.J., 1999, Parallel numerical simulation of subsonic cavity noise, AIAA Paper 99-1891.